Article

Cell

Global Brain Dynamics Embed the Motor Command Sequence of *Caenorhabditis elegans*

Graphical Abstract

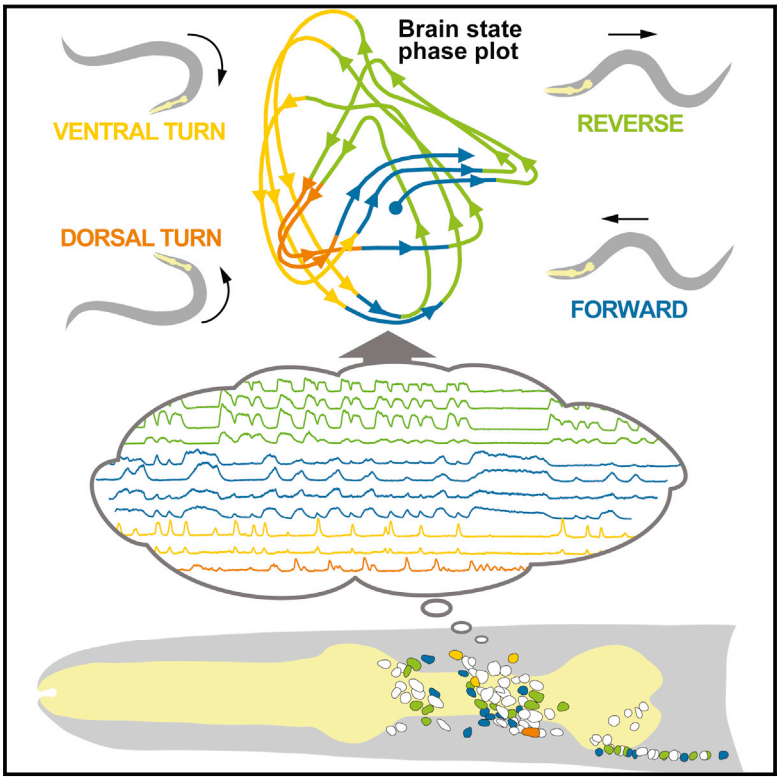

Highlights

- Most active neurons in the brain participate in coordinated dynamical activity
- Smooth, cyclical dynamics continuously represent action sequences and decisions
- Internal representation of behavior persists when de-coupled from its execution
- Brain dynamics provide a robust scaffold for sensory-driven action selection

Authors

Saul Kato, Harris S. Kaplan, Tina Schrödel, ..., Eviatar Yemini, Shawn Lockery, Manuel Zimmer

Correspondence

zimmer@imp.ac.at

In Brief

Simultaneously recording the activity of nearly all neurons in the *C. elegans* brain reveals that most active neurons share information by engaging in coordinated, dynamical network activity that corresponds to the sequential assembly of motor commands.

Kato et al., 2015, Cell *163*, 1–14
October 22, 2015 ©2015 Elsevier Inc.
http://dx.doi.org/10.1016/j.cell.2015.09.034

CellPress

Please cite this article in press as: Kato et al., Global Brain Dynamics Embed the Motor Command Sequence of *Caenorhabditis elegans*, Cell (2015), http://dx.doi.org/10.1016/j.cell.2015.09.034

Article

Cell

Global Brain Dynamics Embed the Motor Command Sequence of *Caenorhabditis elegans*

Saul Kato,[1,4] Harris S. Kaplan,[1,4] Tina Schrödel,[1,4] Susanne Skora,[1] Theodore H. Lindsay,[2,5] Eviatar Yemini,[3] Shawn Lockery,[2] and Manuel Zimmer[1,*]

[1]Research Institute of Molecular Pathology IMP, Vienna Biocenter VBC, Dr. Bohr-Gasse 7, 1030 Vienna, Austria

[2]Institute of Neuroscience, University of Oregon, Eugene, OR 97403, USA

[3]Department of Biochemistry and Molecular Biophysics, Howard Hughes Medical Institute, Columbia University Medical Center, New York, NY 10032, USA

[4]Co-first author

[5]Present address: Division of Biology and Biological Engineering, California Institute of Technology, Pasadena, CA 91125, USA

*Correspondence: zimmer@imp.ac.at

http://dx.doi.org/10.1016/j.cell.2015.09.034

SUMMARY

While isolated motor actions can be correlated with activities of neuronal networks, an unresolved problem is how the brain assembles these activities into organized behaviors like action sequences. Using brain-wide calcium imaging in *Caenorhabditis elegans*, we show that a large proportion of neurons across the brain share information by engaging in coordinated, dynamical network activity. This brain state evolves on a cycle, each segment of which recruits the activities of different neuronal sub-populations and can be explicitly mapped, on a single trial basis, to the animals' major motor commands. This organization defines the assembly of motor commands into a string of run-and-turn action sequence cycles, including decisions between alternative behaviors. These dynamics serve as a robust scaffold for action selection in response to sensory input. This study shows that the coordination of neuronal activity patterns into global brain dynamics underlies the high-level organization of behavior.

INTRODUCTION

Behavior is composed of individual motor actions and motifs, such as limb movements or gaits, which do not achieve organismal goals unless they are orchestrated into longer-lasting action sequences and behavioral strategies, like navigation, grooming, or courtship (Anderson and Perona, 2014; Gray et al., 2005; Seeds et al., 2014). Ethologists often make quantitative descriptions of this higher-level organization using state transition diagrams, consisting of distinct, repeatable high-level motor states and switches between them (Anderson and Perona, 2014). The brain's representation of behavior must account for both detailed metrics of individual actions (e.g., strength and extent of movement or speed of gait), as well as for their higher level orchestration. Identifying how these aspects of behavior correspond to measurable neural activity is a necessary step toward understanding how the brain encodes and produces behavior. Recent studies in invertebrate motor ganglia and mammalian cortex show that selection, execution, and shaping of motor programs correspond to neural activity patterns across large neuronal populations. These studies show that, despite the participation of hundreds of sampled neurons, their activity is coordinated, and meaningful signals can thus be reduced to far fewer dimensions. Moreover, neuronal populations encode information dynamically (Briggman et al., 2005; Bruno et al., 2015; Churchland et al., 2012; Cunningham and Yu, 2014; Harvey et al., 2012; Jin et al., 2014; Mante et al., 2013). For practical reasons, recordings in these studies have been performed over short intervals that encompass individual motions or brief behavioral tasks. Hence, the neuronal mechanisms that govern the continuous control of behavior and its time course, encompassing long-lasting and repeated action sequences, remain enigmatic. Furthermore, approaches have been typically limited by the need to average across trials or to sub-sample from local brain regions or motor ganglia. Recently, the first brain-wide single-cell-resolution functional imaging studies, in zebrafish and fly larvae and adult *C. elegans*, revealed motor-related population dynamics correlated across distant brain regions. These data suggest that behaviorally relevant neural representations might occur at the level of global population dynamics and highlight the benefit of brain-wide sampling (Ahrens et al., 2012, 2013; Lemon et al., 2015; Panier et al., 2013; Prevedel et al., 2014; Schrödel et al., 2013).

The nematode *C. elegans* is an attractive model system to address these problems, due to its stereotypic nervous system of just 302 identifiable neurons grouped into 118 anatomical symmetry classes (White et al., 1986). However, prior to the availability of whole-brain imaging, past studies had not explored distributed or population dynamics in *C. elegans*. Instead, identified interneurons and pre-motor neurons have been described as dedicated encoders of specific sensory inputs or motor outputs and are commonly placed in a context of isolated sensory-to-motor pathways (see the following references for examples: Chalasani et al., 2007; Donnelly et al., 2013; Gray et al., 2005; Ha et al., 2010; Iino and Yoshida, 2009; Kimata et al., 2012). However, these pathways largely overlap and are embedded in a horizontally organized and recurrently connected neuronal wiring diagram (Varshney et al., 2011; White et al., 1986). Moreover, recent functional imaging

Please cite this article in press as: Kato et al., Global Brain Dynamics Embed the Motor Command Sequence of *Caenorhabditis elegans*, Cell (2015), http://dx.doi.org/10.1016/j.cell.2015.09.034

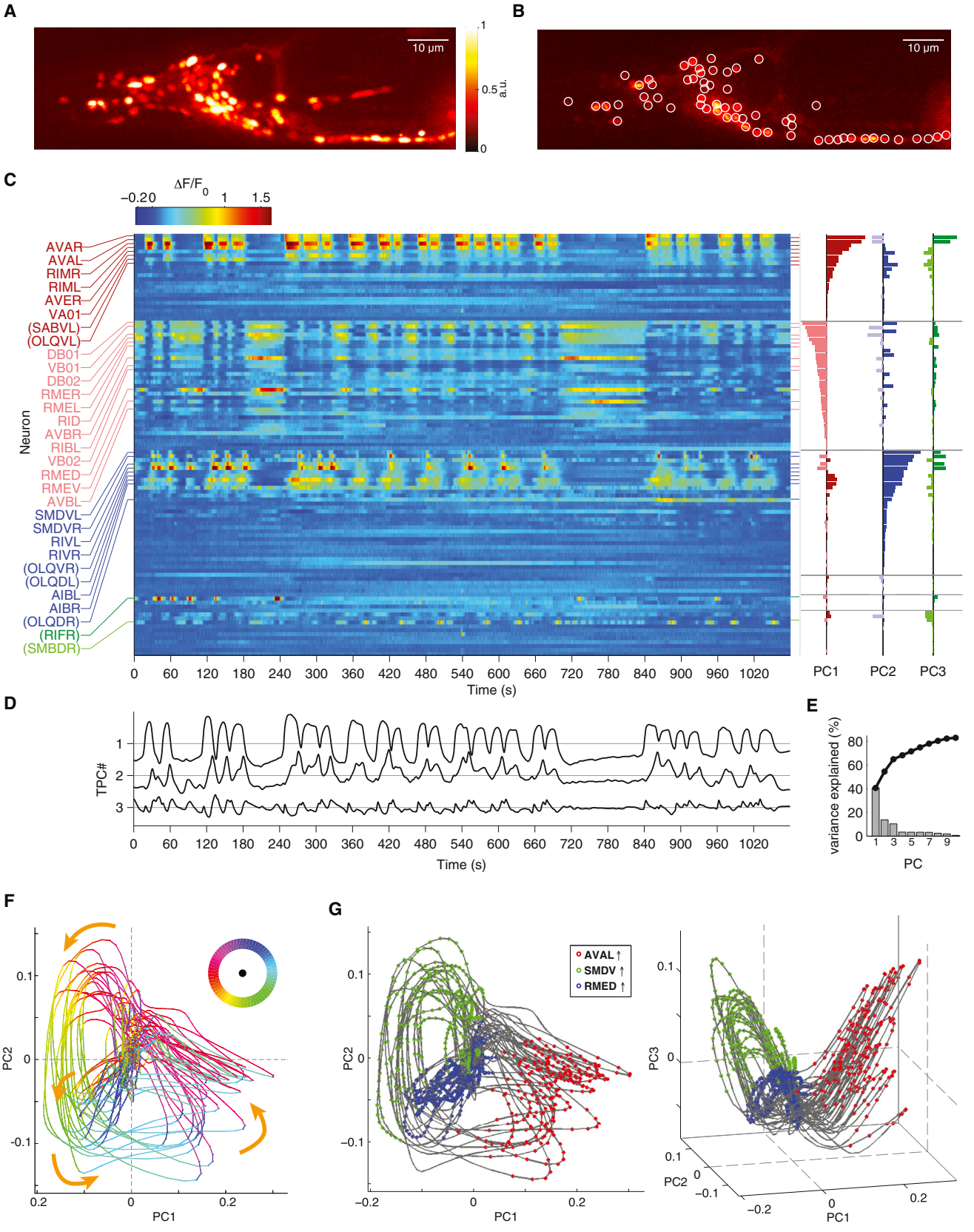

(legend on next page)

studies revealed that many of these circuit elements encode motor rather than sensory related signals (Gordus et al., 2015; Hendricks et al., 2012; Laurent et al., 2015; Li et al., 2014; Luo et al., 2014). Taken together, these considerations argue against separable feed-forward sensory pathways and instead support the hypothesis that sensorimotor processing is performed by distributed, shared networks operating on widespread motor representations.

In the present study, we provide evidence for this hypothesis by showing that many neurons in the *C. elegans* brain participate in a pervasive dynamic population state, collectively representing the major motor commands of the animal. The time evolution of the neural state is directional and cyclical, corresponding to the sequential order of the animals' repeated actions. These network dynamics interface with sensory representations as early as at the first synapse downstream of sensory neurons and provide a robust scaffold for sensory inputs to modulate behavior. Our work suggests that high-level organization of behavior is encoded in the brain by globally distributed, continuous, and low-dimensional dynamics.

RESULTS

Brain-wide Activity Evolves on a Low-Dimensional Attractor-like Manifold

We performed whole-brain single-cell-resolution Ca^{2+} imaging with a pan-neuronally expressed nuclear Ca^{2+} sensor in animals immobilized in a microfluidic device (Schrödel et al., 2013). In each animal (n = 5), we recorded the brain activity under environmentally constant conditions for 18 min at a rate of ~2.85 volumes per second. The imaging volume spanned all head ganglia, including most of the worm's sensory neurons and interneurons, as well as all head motor neurons and the most anterior ventral cord motor neurons (White et al., 1986) (Figures 1A and 1B). In each recording, we detected 107–131 neurons and were able to determine the cell class identity of most of the active neurons. Figures 1C and S1A show a typical multi-neuron time series during which a large proportion of imaged neurons exhibited discernable Ca^{2+}-activity patterns. We performed principal components analysis (PCA) on the time derivatives of the normalized Ca^{2+} traces (Figures 1C–1E). This method produces neuron weight vectors, termed principal components (PCs); here, PCs are calculated based on the covariance structure found in the normalized data (Jolliffe, 2002). For each PC, a corresponding time series (temporal PC) was calculated by taking the weighted average of the full multi-neural time series. Temporal PCs represent signals shared by neurons that cluster based on their correlations. We found a low-dimensional, widely shared, dominant signal: the first three PCs accounted for 65% of the full dataset variance (Figure 1E). We performed PCA on the time derivatives of Ca^{2+} traces because the resulting PCs produced more spatially organized state space trajectories, described below.

The time integral of temporal PC1 displayed a strong oscillatory time course with variable period, sharp transitions, and prolonged plateaus and troughs. This pattern derived from the antagonistic activity of two groups of interneurons and motor neurons (Figure 1C, right) previously implicated in controlling the switch between forward- and backward-directed crawling (Table S1 summarizes published results). Neurons previously reported to have opposing roles were observed to have opposing signs of their PC1 weights—e.g., AVA promoting backward crawling and AVB promoting forward crawling. PC2 and PC3 received high contributions from head motor neurons. Two of these neurons (SMDV and RIV) have been implicated in postural changes required for navigational re-orientation maneuvers (termed omega turns) (Gray et al., 2005). However, the neuronal weights of all three PCs indicated contributions from many neurons (Figure 1C). PC1–3 weights and their variance contributions were consistent across the five datasets (Figures S2A–S2D).

The phase plot of temporal PC1–3 showed that the neural state's time evolution was cyclical—i.e., the same states were repeatedly revisited within a trial, such that successive trajectory cycles formed spatially coherent bundles (Figure 1F and Movie S1). Consequently, the entire neural state trajectory traced out a manifold, which is defined here as the sub-volume in PCA space occupied by the neural state trajectory. When mapped onto the neural trajectory, individual neurons' activity rise and fall phases occupied class-specific sub-regions on the manifold (Figures 1G and S1B). All five recordings displayed a similarly structured manifold (Figure S2E). Thus, a large group of interneurons and motor neurons produces a cyclical, low-dimensional population state time-varying signal.

Interneurons and Head Motor Neurons Reliably Encode Motor State and Graded Motion Parameters

Next, we aimed for a functional interpretation of the neural state manifold and its properties. Each manifold sub-region was labeled specifically and consistently by different subsets of neurons, some of which have been previously implicated in the action sequence termed a pirouette (Table S1), which is central to navigation (Gray et al., 2005; Pierce-Shimomura et al., 1999). During pirouettes, worms switch transiently from

Figure 1. Brain-wide Activity Is Organized in a Low-Dimensional, Cyclical Neural State Space Trajectory

(A) Maximum intensity projection of a representative sample recorded under constant conditions.

(B) Single z plane overlaid with segmented neuronal regions.

(C) Heat plot of fluorescence ($\Delta F/F$) time series of 109 segmented head neurons, one neuron per row. Labeled neurons indicate putative cell IDs. Ambiguous neuron IDs are in parentheses (see Figure S1 for additional candidates). Neurons are colored and grouped by their principal component (PC1–3) weights and signs, which are shown by the bar plots on the right.

(D) Integrals of the first three temporal PCs.

(E) Variance explained by first ten PCs, black line indicates cumulative variance explained.

(F) Phase plot of first two temporal PCs colored by direction of time evolution indicated by color key.

(G) Phase plots of first two (left) and first three (right) temporal PCs. Colored balls indicate Ca^{2+} rises of three example neurons indicated by legend.

See also Movie S1 and Figures S1 and S2.

forward- to backward-directed crawling, termed a reversal (Figures 2A and 2B). They then resume forward crawling with a concomitant turn along the dorsal or ventral body axis; worms crawl lying on their left or right side (Figures 2C and 2D). We performed Ca^{2+} imaging experiments of representative neurons in freely moving worms while simultaneously recording their behavior with an infrared (IR) camera (Faumont et al., 2011). We selected neurons based on their PC weights and availability of specific promoters to drive GCaMP expression. As with brain-wide imaging experiments, animals were recorded 5–10 min after removal from food, a paradigm in which pirouettes contribute to a local search strategy (Gray et al., 2005). Behavioral analysis of the IR movies showed that reversal initiations were each preceded by a reduction in crawling speed (slowing bout), though 20% of slowing bouts did not lead to a reversal (Figures S3A and S3B). We thus defined slowing as an additional behavioral state and represent pirouettes together with forward crawling as action sequences composed of forward run, slowing, reversal, resume forward via dorsal turn, and resume forward via ventral turn actions, which is depicted in a state transition diagram (Figure 2E).

We first examined Ca^{2+} dynamics in neurons with high positive or negative PC1 weight. An example trace of RIM neurons is shown in Figure 2F. We found that the Ca^{2+} signals of RIM resided in stable low states during forward-directed crawling and that Ca^{2+} rises occurred exclusively during reversals (Figure 2F). The slope of these signals correlated with the speed of reverse crawling (Figure 2G). Although reversals are of variable duration (Gray et al., 2005; Pokala et al., 2014) (Figure S3B), RIM Ca^{2+} rise onsets precisely aligned with reversal start, and RIM Ca^{2+} fall onsets aligned with reversal end. This relationship was highly reliable—approximately 90% of reversals were associated with a detectable RIM Ca^{2+} rise phase (Figure 2H, top), and the remainders were very short reversals where small Ca^{2+} signals might have been occluded by noise (Figure 2F). All clearly discernible RIM Ca^{2+} rises above our signal-to-noise threshold occurred during reversals. We found such a relationship of Ca^{2+} rise and fall phases with respect to reversal events for all tested neurons with positive PC1 weight (RIM, AVA, AVE, AIB), while neurons with negative PC1 weight (RIB, AVB, RMEV) showed the inverse relationship (Figures 2H and S3C–S3H). All these neurons' activities changed as reliably as RIM at both forward-reverse and reverse-forward transitions.

Besides this common property of PC1 neurons, class-specific relationships between neuronal activity and locomotion were revealed by freely moving Ca^{2+} imaging. RIM and AVA Ca^{2+} rise slopes, and AVE Ca^{2+} signal magnitude, were graded and correlated with reverse crawling speed (Figures 2G, S3I, and S3J). Unlike RIM, AVA, and AVE, the activity of AIB did not show strong correlations with reverse crawling speed (Figures S3E and S3K); however, small AIB Ca^{2+} transients co-occurred with forward slowing bouts, even when no reversal followed (Figures S3E and S3Q). Consistent with this, AIB Ca^{2+} rise phases preceded the forward-to-reversal transition by ~1 s on average (Figure 2H). The continuous activity of AVB and RIB, unlike RMEV, showed strong correlations with forward crawling speed (Figures S3L–S3P; see also Li et al., 2014). Consistent with this, AVB and RIB Ca^{2+} fall phases preceded the forward to reverse transition by ~1 s on average (Figure 2H).

Next, we examined the activity of SMDV head motor neurons as representative neurons with strong PC2/3 weight. Resumption of forward crawling begins with a dorsal or ventral bend, which was biased (71%/29%) in the ventral direction. The head flexure during post-reversal turns is graded and increased compared to normal forward crawling, especially for ventral bends (Figure 3A). SMDV exhibited Ca^{2+} rises at the transition from reverse to forward crawling; importantly, these rises occurred exclusively during ventrally and not dorsally directed events (Figures 3B–3D). The magnitude of these signals correlated with ventral head-bending flexure (Figure 3E).

The major qualitative divergence in neural activity patterns between the freely moving single neuron and restrained whole-brain setups that we observed was the absence, in freely moving worms, of prolonged high phases in neurons with positive PC1 weight. Using RIM as an exemplar, we first ruled out that this difference was a consequence of nuclear localization of the Ca^{2+} reporter used in whole-brain imaging (Figures S3R–S3T). We then dissociated the two major differences in these experimental conditions by performing experiments in either pharmacologically or physically immobilized worms. While low doses of the paralyzing agent tetramisole caused RIM high phases in conjunction with prolonged slowly executed reversals, physical immobilization alone also caused RIM high phases (Figures S3U–S3X). These data suggest that impeded motor execution leads to a prolongation of the reversal, which is correlated with sustained Ca^{2+} levels in reversal-promoting neurons.

In summary, the investigated neuronal activities showed both (1) sharp transitions depending on discrete motor state (i.e., forward versus backward crawling, ventral versus dorsal turning direction) and (2) graded information about motion parameters (i.e., forward and reverse crawling speed and head bending flexure). Acute motor state reliably matched the activities of the associated neurons on a single event basis. Importantly, when examining neuron activity periods mapped onto the neural state manifold, we observed that neurons encoding the same behavioral state in freely moving animals shared the same manifold sub-regions with rare exception (Figure S1B).

Manifold Branches and Bundles Exhibit Distinct Neuronal Recruitment Patterns

Having determined that the neural state manifold is a composite of motor related signals, we next aimed for a quantitative description thereof. We first segmented the global brain cycle into four behaviorally relevant phases using the left AVA neuron (AVAL) as a reference: a trough in AVAL Ca^{2+} defined the LOW state, a Ca^{2+} increase the RISE state, a Ca^{2+} plateau the HIGH state, and a Ca^{2+} decrease the FALL state (Figure 4A). We chose this single neuron class because it is among the highest PC1 contributors, participated in every brain cycle, and, unlike temporal PCs, exhibited sharply discernible transitions; however, other strongly PC1-contributing neurons such as RIM could also be used for this purpose. We validated that the appearance of lasting plateau and smooth transition states was not due to temporal filtering effects of Ca^{2+} imaging: all four states were readily discernible in AVA membrane voltage recordings, and

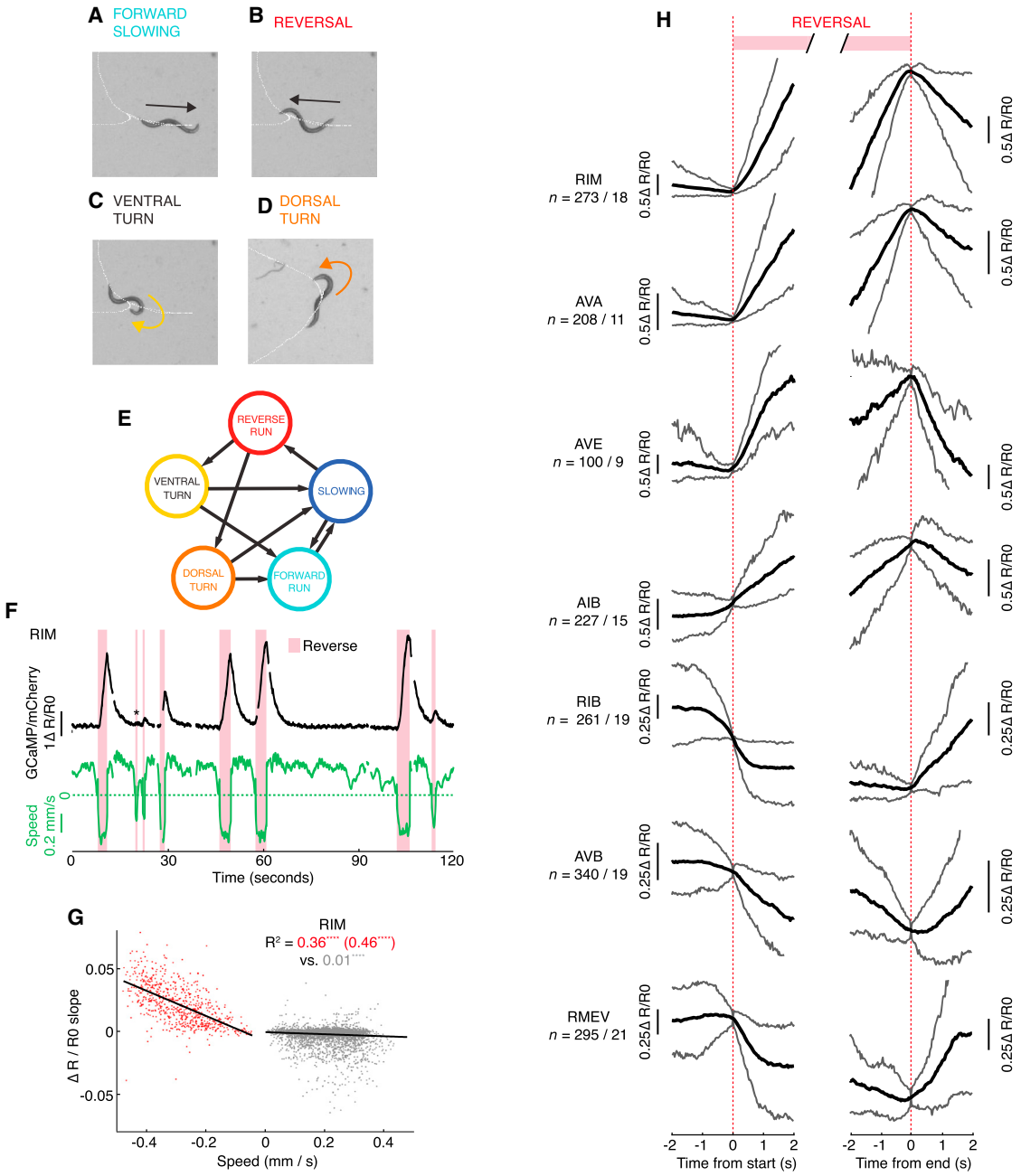

Figure 2. Distributed Encoding of Motor State and Crawling Speed by Interneurons in Freely Moving Worms

(A–D) Motor states of pirouette action sequence. White dotted lines show crawling trajectory. Arrows indicate crawling direction.

(E) Behavioral state transition diagram indicating motor states as circles and possible transitions as arrows.

(F–H) Ca^{2+} imaging in freely moving animals.

(F) Example trace showing RIM activity as normalized GCaMP/mCherry fluorescence ratio (black) and corresponding crawling speed (green). Pink bars overlay reverse crawling periods. Asterisk indicates reversal with no detectable RIM activity peak.

(G) Regression analysis of crawling speed versus RIM Ca^{2+} signal slope. R^2 indicates goodness of linear fit for instantaneous and maximum (in parentheses) reverse speed (red) and instantaneous forward speed (gray). Permutation test p value ****$p < 0.0001$ indicates probability that correlation was obtained by chance.

(H) Average Ca^{2+} signals of the indicated neurons triggered to reversal start (left) or end (right). Upper and lower traces represent 90th and 10th percentile of all data, respectively. Number of recorded worms and reversal events are indicated.

See also Figure S3.

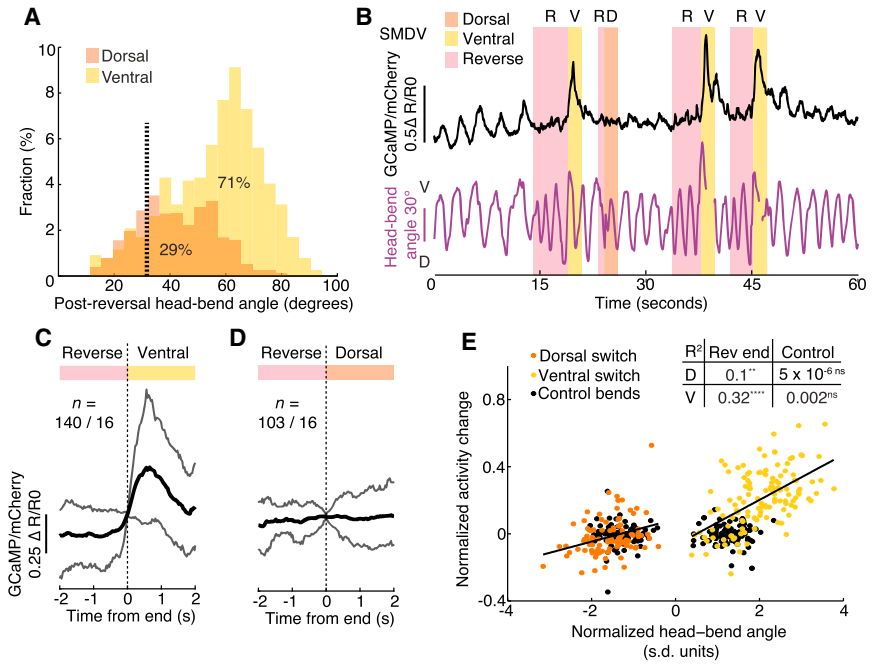

Figure 3. SMDV Signals during Ventral, but Not Dorsal, Post-Reversal Turns

(A) Fractional histogram showing postural angle of first post-reversal head bend (ventral, yellow; dorsal, orange). Numbers indicate percentage of all post reversal head bends. Dashed vertical black line shows median of all other head bends (no difference between ventral and dorsal).

(B–E) SMDV Ca^{2+} imaging in freely moving animals.

(B) Example trace showing SMDV activity as normalized GCaMP/mCherry fluorescence ratio (black) and corresponding head-bend angle (purple). Pink bars overlay reverse crawling; yellow and orange bars overlay ventral and dorsal post-reversal head-bends, respectively.

(C and D) Average SMDV Ca^{2+} signals triggered to reversals ending with ventral (C) or dorsal (D) head bends. Upper and lower traces represent 90th and 10th percentile of all data, respectively. Number of recorded worms and events are indicated.

(E) Regression analysis of normalized peak post-reversal head-bend angle versus SMDV Ca^{2+} signal. Ventral and dorsal bends are shown in yellow and orange, respectively. Black open circles show an equal number of randomly selected head-bend peaks during regular forward movement. R^2 indicates goodness of linear fits to ventral (V), dorsal (D), and respective control groups. Permutation test p values (****$p < 0.0001$, **$p < 0.01$, ^{ns} not significant) indicate probability that R^2 value was obtained by chance.

we calculated an estimate of low-pass filtering caused by nuclear Ca^{2+}-imaging, producing a maximum delay in signal peaks of less than 1.1 s (Figure S4). Although neurons with a common relationship to behavior were recruited to the same sub-regions of the manifold, their precise phase onsets and offsets varied. In order to quantify this observation, for each onset of RISE and FALL, we created a vector containing the phase delays of all recruited neurons (Figure S5) (see Supplemental Experimental Procedures for details). Across the five datasets, we detected 121 RISE and 123 FALL transitions and observed characteristic phase delay distributions for each neuronal class (Figure S5). Next, we searched for structure across neuronal classes by performing k-means clustering separately for the RISE and FALL phase timing vectors; we found that both could be significantly clustered into two groups each, which we termed RISE1/2 and FALL1/2, respectively. RISE1 differed from RISE2 mostly based on different timing of neurons; e.g., AIB and RIB activity exhibited phase advances during RISE1 (Figure S5). FALL1 and FALL2 mostly differed by mutually exclusive head motor neuron recruitments, SMDV/RIV versus RMED/ventral ganglion head motor neuron (likely SMB, SMDD, or RMF) (Figure S5). The precise ordering detected by this method may be affected by differential Ca^{2+} dynamics in different cells; however, the reproducible clustering would be preserved. Using this six-state classification (LOW, RISE1/2, HIGH, and FALL1/2), we labeled the neural state trajectory and found that each state classifies a distinct bundle of trajectory segments (Figures 4A and 4B and Movie S2). Thus, the two methods (PCA and phase timing analysis) revealed the same dynamical structure in the neural data. Bundle classification enabled us to calculate average neural state trajectories illustrating the canonical brain cycle (Figure 4C). Note that, without this single-trial clustering analysis, the cycle-averaged trajectory would be reduced to a single loop in neural state space. Furthermore, bundle classification enabled us to estimate a contour surface of the manifold (Figure 4D and Movie S3), where the extents correspond to the standard deviations (SDs) by which the trajectory path diverges from the canonical (average) path. The trajectory segments across all cycles are strongly bundled; the mean pairwise distance of points across any two phase-registered trajectory time points within a bundle is ~10% of the diameter of the full trajectory, and their mean angular divergence is 22° versus 90° expected from uncorrelated orientations. In summary, we find that many active neurons across the brain are tightly bound to reproducible and smooth population dynamics.

The Motor Command Sequence Is Embedded in Neural State Space

Remarkably, the relationships neurons exhibited with behavioral transitions (Figures 2H, 3C, and 3D) matched their phase relationships with the six state global brain cycle without exception. Assembling all of the neuronal-behavioral correlate information gathered via Ca^{2+} imaging in freely moving worms enabled us to unambiguously map the worm's major motor command states onto separate bundles of the neural state manifold (Figures 4B–4E)—RISE1 or RISE2, in conjunction with HIGH, correspond to reversals, with HIGH corresponding to the sustained reversal seen only in immobilized animals. FALL1 corresponds to the post-reversal ventral turn and FALL2 to the dorsal turn. FALL1 and FALL2, in conjunction with LOW, correspond to forward crawling. Slowing mapped to final sections of LOW

preceding RISEs (Figures 4B–4E, see Experimental Procedures for the detailed mapping rules). Thus, the neural state manifold, on a single trial basis, embeds the pirouette command sequence described in the state transition diagram (Figures 2A–2E). The neural trajectory follows the same unidirectional sequence through manifold sub-regions as the corresponding behavioral sequence executed by freely moving worms during pirouettes. This observation motivated us to redraw the state transition diagram (Figure 2E) as a continuous flow graph (Figure 4E). The neuronal manifold, in addition to embedding the command sequence, also contains information about graded locomotion parameters like the drive underlying crawling speed (Figure 4F, see Experimental Procedures for the detailed mapping rules). Both motor command states, as well as speed drive, appear organized on the manifold; i.e., separable sub-regions unambiguously delimit the distinct command states (Figure 4B) and proximal traversals on the manifold exhibit similar speed drives (Figure 4F). This manifold organization was clearly apparent in all five recordings (Figure S2E).

Each branching region of the manifold represents a decision where the subsequent motor state is determined. To explore the process of decision execution, we quantified the time course of trajectory separation when branching into RISE1 versus RISE2 and FALL1 versus FALL2 and subsequent merging. This approach calculates how significantly trajectory segments bundle in PCA space when tested against random shuffling of membership in RISE1 versus RISE2 or FALL1 versus FALL2 clusters (see Supplemental Experimental Procedures for details). Consistent with the significant clustering of neuronal recruitment vectors described above, there was significant separation during the RISE and FALL phases (Figures 4G and 4H). Interestingly, this also uncovered memory effects: a RISE1 versus RISE2 branch choice could, on average, be predicted during the preceding FALL period (Figure 4G), and consistent with the previous, FALL1 versus FALL2 trajectories remained significantly unmixed in the following RISE phases (Figure 4H). Moreover, RISE1 and RISE2 are associated, respectively, with long and short preceding LOW states (Figure 4I). Both results indicate that the trajectory path history influences the future branch choice decision.

In contrast to the state transition diagram, the neural state manifold captures the continuous dynamical structure of motor commands and their transitions and contains additional information about graded metrics of motion, like crawling speed and postural flexure. Here, we define the terms command state and speed drive as the brain's internal high-level representations of the underlying motor programs, since these are readily observable in immobilized animals in the absence of motor execution.

Neural State Dynamics Persist When a Hub Output Neuron Is Inhibited

The presence of a representation of the pirouette sequence in immobilized animals suggests that the neuronal population dynamics are primarily internally driven and thus represent descending motor commands that can operate in the absence of motor feedback. We sought to further test this hypothesis. Despite the largely recurrent connectivity of the *C. elegans* wiring diagram, a bottleneck exists from the head ganglia to body motor neurons—AVA pre-motor interneurons are anatomical network hubs linking head ganglia neurons to A-class ventral cord motor neurons, which mediate the reversal motor program (Chalfie et al., 1985; Kawano et al., 2011; Varshney et al., 2011). Acutely silencing AVA via transgenic expression of a histamine-gated chloride channel (HisCl) (Pokala et al., 2014) abolished reversals in freely moving worms (Figure 5A). As expected, similarly silenced animals under whole-brain imaging (n = 5 recordings) showed substantial attenuation of AVA activity and strong uncoupling of AVA from the global brain cycle (Figures 5B and S6A). Additionally, activity of the reverse interneurons AVE and RIM, which are connected to AVA via gap junctions (White et al., 1986) was slightly attenuated (Figure 5B). However, their phase relationships with most other neurons appeared normal (Figure S6C). A-class ventral cord motor neurons, the principal output targets of AVA, also showed significant attenuation (Figure 5B). Despite these effects, the cyclical dynamics and neuronal recruitment patterns were largely preserved (Figures 5C, 5D, and S6). The distributions of network state durations were unchanged, with the exception of a decrease in HIGH state duration, suggesting that network HIGH state prolongation was due in part to reinforcement from AVA (Figure 5E). These observations raised the possibility that the global brain cycle was also intact in freely moving worms with AVA, and therefore reversals, inhibited. Unlike in wild-type animals, where 92.5% of turns occurred in conjunction with a preceding reversal, in worms with silenced AVA neurons, none of the turns were preceded by reversals; instead, 68% of turns (32 out of 47) were preceded by prolonged slowing or pauses, while the rest occurred during apparently normal forward locomotion. Imaging RIM in AVA-silenced freely moving animals revealed the presence of sustained RIM activity during these prolonged slowing or pauses preceding normal turning events (Figures 5F–5H). Such transients were never seen in controls, where RIM was only active during reversals. In AVA-silenced animals, RIM activity often entered HIGH states during prolonged pauses, further supporting the above interpretation that the HIGH state occurs due to the absence of effectual motor execution (Figures 5F and S3U–S3X). These results show that the cyclical time course of the brain-wide motor command is maintained in the absence of reversal execution, the only effect of which is a prolonged HIGH state duration. Analogously, behaviors that are not AVA-output mediated (slowing and turns) are also preserved. Further, these data imply that AVA is not a privileged generator of motor commands but should instead be characterized as an output-facing member of the collectively oscillating interneuron group.

Entrainment of the Global Brain Cycle by Sensory Stimulation

Next, we investigated how these collective network dynamics interact with a chemosensory input. Under whole-brain imaging, we stimulated oxygen chemosensory neurons with consecutive oxygen up- and down-shifts (21% versus 4%), a protocol previously shown to reliably activate BAG, URX, and AQR oxygen sensory neurons and to entrain pirouette behavior with high pirouette probability at 21% oxygen and low at 4% (Figures S7A and S7B; see also references Busch et al., 2012; Schrödel et al., 2013; Zimmer et al., 2009). To our surprise, with the exception of one ventral ganglion neuron class (RIG or RIF)

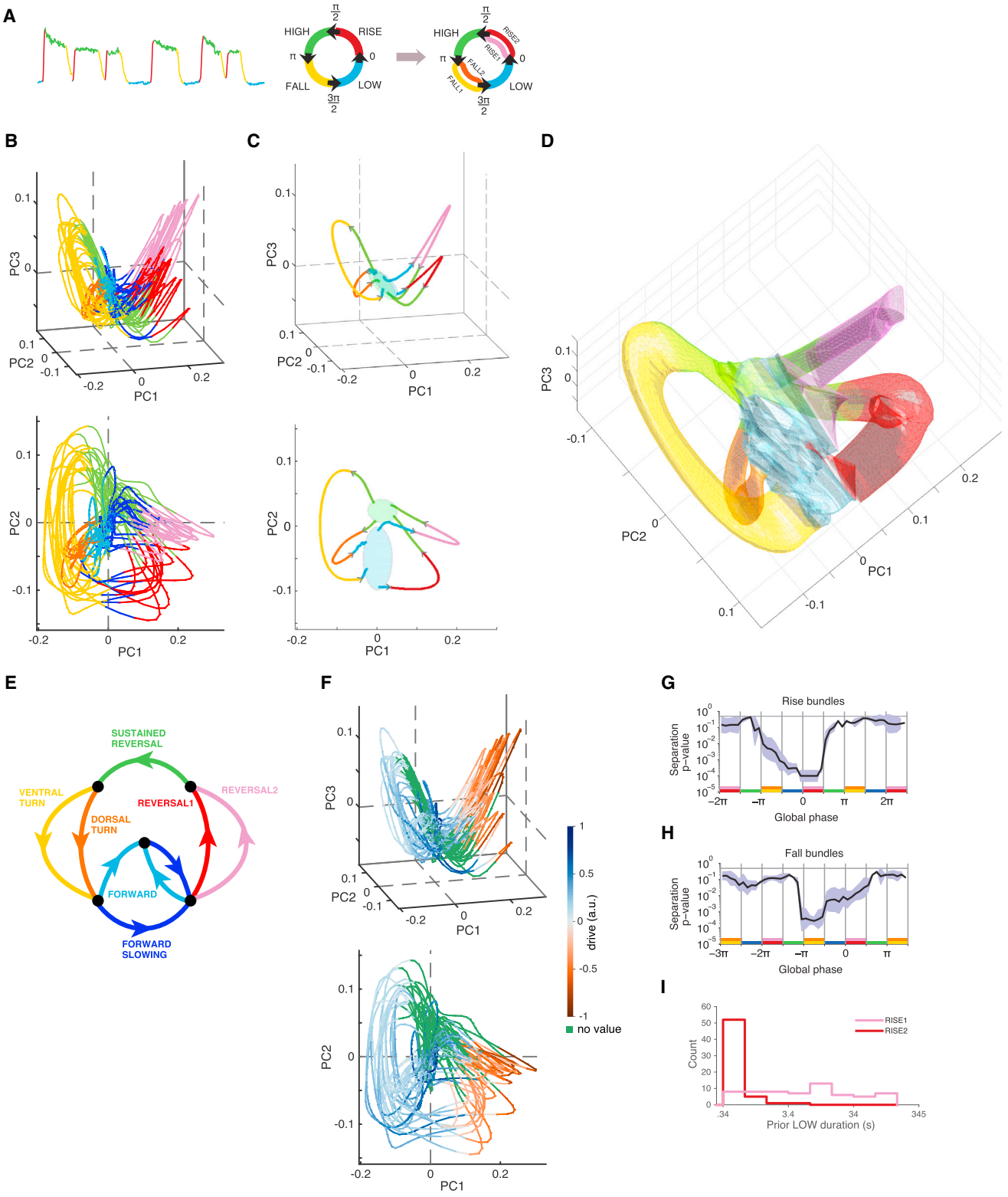

Figure 4. The Neural State Manifold Embeds the Action Sequence and Exhibits Organized Analog Speed Drive

(A) Phase segmentation of example AVAL trace (left). Four-state brain cycle (middle). Phase timing analysis and clustering leads to six-state brain cycle (right). See also Figures S4 and S5.

(B) Phase plot of the same trial shown in Figure 1, colored by six-state brain cycle plus FORWARD SLOWING command state in purple (see below).

(legend continued on next page)

(Figure S7C), we did not detect single-neuron representations of sensory stimulus downstream of sensory neurons (n = 13 recordings). Moreover, the topology of the neural state manifold did not change upon stimulation; however, there were some magnitude effects on the amplitude of temporal PC1 (Figure 6A). Based on the strong entrainment effect the stimulation protocol has on pirouette behavior, we expected that oxygen concentration should affect bundle occupancy on the manifold. Indeed, the stimulus protocol entrained the global phase of the brain cycle so that the probability of the reverse motor command state declined during 4% oxygen periods and increased during 21% oxygen periods (Figures 6B and 6C), indicating a successful sensorimotor transformation in our preparation. Consistent with these findings, Ca^{2+} rises in BAG neurons during the HIGH state evoked immediate FALL1 or FALL2 transitions in 56% (30/54, n = 13 recordings) of all instances (see Figure S7C for an example). Interestingly, in 22 out of the 24 remaining instances, secondary BAG Ca^{2+}-rises coincided with a FALL1 or FALL2 transition; these were the only times when we observed secondary BAG transients (see Figure S7C as an example). This finding suggests the existence of a feedback mechanism eliciting or gating secondary Ca^{2+} rises in the BAG sensory neurons, demonstrating that variability in the BAG sensory response profile (Zimmer et al., 2009) can be explained when the underlying brain state is known to the observer.

Finally, we looked for sensory-evoked Ca^{2+} activity in the major PC1 neuron classes AVA, AVE, and RIB in freely moving animals. Together AVE and RIB receive 47% of BAG neuron synapses (White et al., 1986). Consistent with our whole-brain imaging results, these neurons retained a tight correlation with motor state and movement metrics and lacked obvious sensory encoding activity; the magnitude of Ca^{2+} signals was subtly modulated during the stimulation periods (Figures S7D–S7U).

In summary, neural state manifold organization is robust to a salient sensory input and thus stably encodes the motor command sequences of the worm under these conditions. The major effect of sensory input was to modulate the probability that the neural state resides on a particular segment bundle by driving the neural state along a lawful trajectory. The result is an entrainment of the global brain cycle, which is consistent with the entrainment of corresponding motor behaviors in freely moving worms.

DISCUSSION

In this work, we identify and characterize a brain-wide signal in *C. elegans* that dominates the neural activity time series. Although our approach required the use of a nuclear localized Ca^{2+} indicator, omitting the detection of subcellular Ca^{2+} signals (Chalasani et al., 2007; Hendricks et al., 2012; Li et al., 2014), it reveals a pervasive motor state representation that is shared among most interneuron and motor neuron layers. The neural state trajectory exhibits directional, cyclical flow (Figure 1F) confined to a low-dimensional manifold (Figure 4D), organized into bundles (Figures 4B–4D) composed of stereotyped and smoothly changing neural activity vectors (Figure S5). Each motor command within the pirouette action sequence is reliably represented across several neurons. Neurons additionally encode graded parameters of locomotion, e.g., crawling speed and postural flexure (Figures 2, 3, and S3). These data enable us to unambiguously map behavioral commands onto sub-regions of the neural state manifold, enabling instantaneous behavioral decoding throughout an experimental trial (Figures 4B and 4E). We interpret these dynamics as corresponding to motor commands, as they can be decoupled from motor output either by restraint (during whole-brain imaging) or manipulation of a major output neuron (Figure 5). Organized flow along the neural state manifold mediates the assembly of motor commands into action sequences (Figures 4B and 4E); it thus represents the high-level temporal organization of behavior upstream of the generation of the animal's undulatory gait. This contrasts with population dynamics in the motor ganglia of crustaceans, mollusks, and lampreys that generate peristaltic and movement rhythms (Bruno et al., 2015; Grillner, 2006; Marder and Bucher, 2007). Interestingly, the brain's forward and reversal motor commands are coupled to corresponding rise, high, fall, and low states in the B- and A-class ventral nerve cord (VNC) motor neurons (Figures 1 and S1), which is consistent with previous studies performed in moving *C. elegans*. Additionally, VNC motor neuron activity exhibits gait-related rhythmic activity superimposed on these command states (Kawano et al., 2011; Wen et al., 2012), which requires proprioceptive coupling to movement (Wen et al., 2012). Taken together, we propose that behavioral state is encoded in the brain and coupled to the motor periphery and that this coupling co-occurs with locally maintained rhythmic activity.

These continuous neural dynamics embed behavioral motifs, described by the state transition diagram, and permit their superposition with graded motion metrics (Figure 4F). The process of decision making leading to execution of alternate behaviors can be observed as the time evolution of neural trajectories before the branches (Figures 4B–4D, 4G, and 4H). We propose that the phenomenon of global dynamics robustly and continuously encoding action sequence commands may be present in

(C) Phase-registered averages of the two RISE phase and two FALL phase bundles colored by six-state brain cycle. Semi-transparent ovals denote trajectory bundle mixing regions.
(D) Contour surface illustrating the neural state manifold colored by six-state brain cycle.
(E) Flow diagram indicating the motor command states corresponding to the six-state brain cycle plus FORWARD SLOWING command state (purple).
(F) The same phase plot colored by forward- and reverse-speed drive inferred from neural correlate decoding. Green trajectory segments indicate the SUSTAINED REVERSAL state, for which no drive correspondence is made. See Figure S2 for more examples.
(G and H) Quantification of inter-bundle separation and mixing for RISE (G) and FALL (H) clusters. Traces show trial-averaged p values (shading indicates SEM; n = 5 animals) of mean normalized pairwise distance at instantaneous points in the past or future, which indicate the probability that the observed separation between bundles occurred by chance. This calculation was done in six dimensions (PC1–3 plus their derivatives) to incorporate directional information from the trajectory paths.
(I) Distribution of LOW state durations preceding RISE1 or RISE2 segments.
See also Movies S2 and S3.

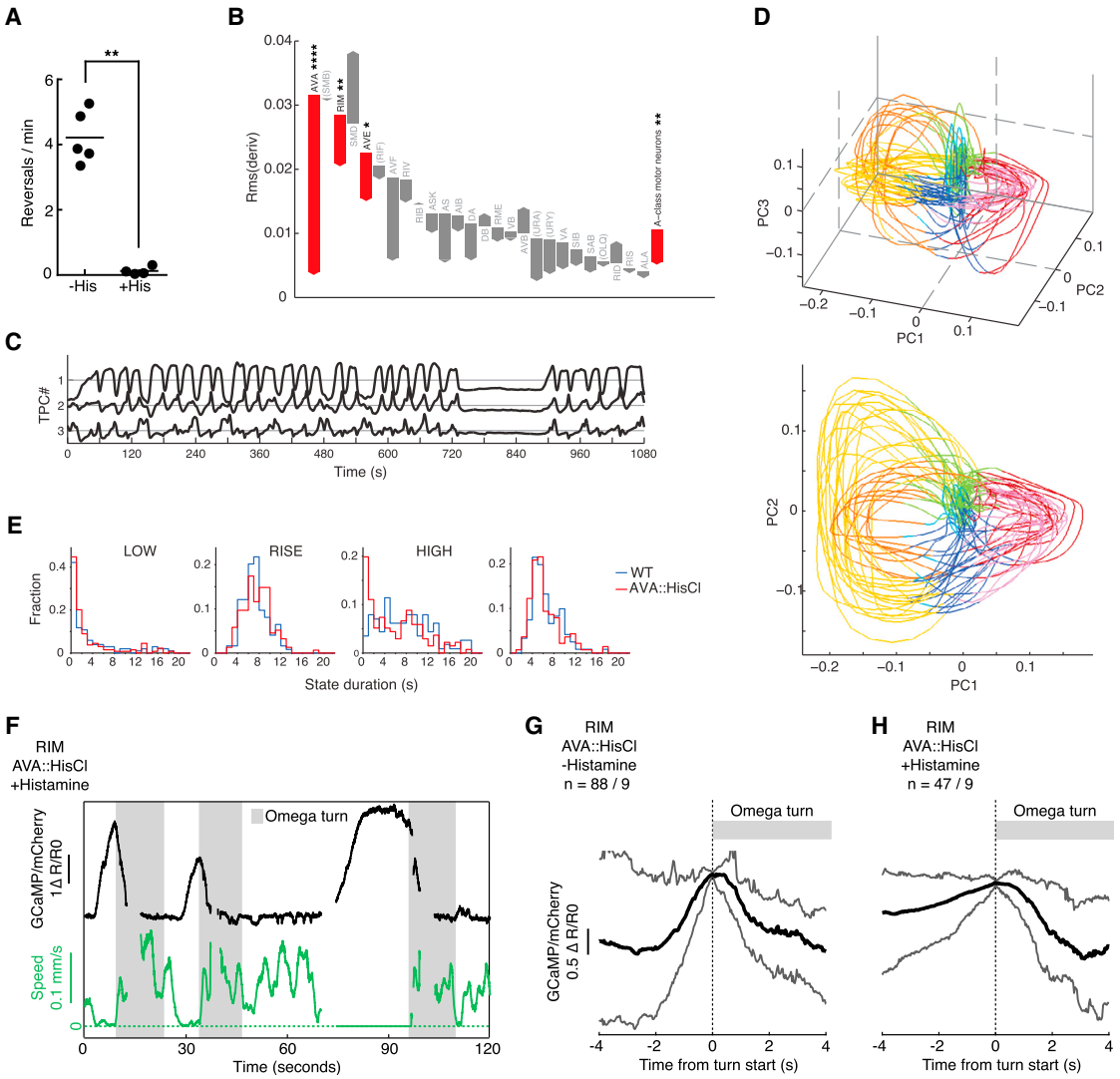

Figure 5. Global Brain Dynamics Persist when Decoupled from Motor Output

(A) Reversal events per minute for AVA::HisCl worms without (−His) or with (+His) histamine treatment. Each data point represents a single assay, n = 20–25 worms per assay. Horizontal lines show means. Mann-Whitney test, $^{**}p < 0.01$.

(B) Shifts in trial-averaged root-mean-squared power of neuronal trace derivatives of AVA::HisCl worms with histamine treatment, relative to wild-type control (n = 5). Gray bars indicate non-significant power shifts, red bars indicate significant power shifts. Class-A motor neurons, typically 1–2 visible per recording, were combined. Significance was determined using a permutation test, $^{****}p < 0.0001$, $^{**}p < 0.01$, $^{*}p < 0.05$.

(C and D) Integrated temporal PCs (C) and phase plots (D) of an example AVA::HisCl dataset.

(E) Distributions of state durations of AVA::HisCl (red) versus wild-type (blue) across multiple trials (n = 5).

(F–H) Ca^{2+} imaging of RIM in freely moving animals expressing HisCl in AVA.

(F) Example trace showing RIM activity in an AVA::HisCl worm after histamine treatment. Normalized GCaMP/mCherry fluorescence ratio (black) and corresponding crawling speed (green) are shown. Omega turns are indicated with gray overlaid bars. These worms did not exhibit reversals.

(G and H) Averages of RIM Ca^{2+} signals in AVA::HisCl worms triggered to omega turn onset, for worms pre-incubated without (G) or with (H) histamine. Upper and lower traces represent 90th and 10th percentile of all data, respectively. Number of recorded worms and omega turns are indicated.

See also Figure S6.

higher animals with more sophisticated behavioral repertoires. This hypothesis is supported by the observation of smooth population dynamics maintaining navigational plans in rodents (Harvey et al., 2012). Its generality could be further tested by studying the basis of well-described sequential courtship and grooming behaviors in fruit flies (Dankert et al., 2009; Seeds et al., 2014). The ability to find dynamical structure solely on the basis of neural event timing (Figure S5) suggests that the structure we observe is not a particular consequence of the graded, non-spiking, nature of *C. elegans* neurons. We speculate that neuronal population trajectories associated with action selection in leeches (Briggman et al., 2005), limb movement in monkey

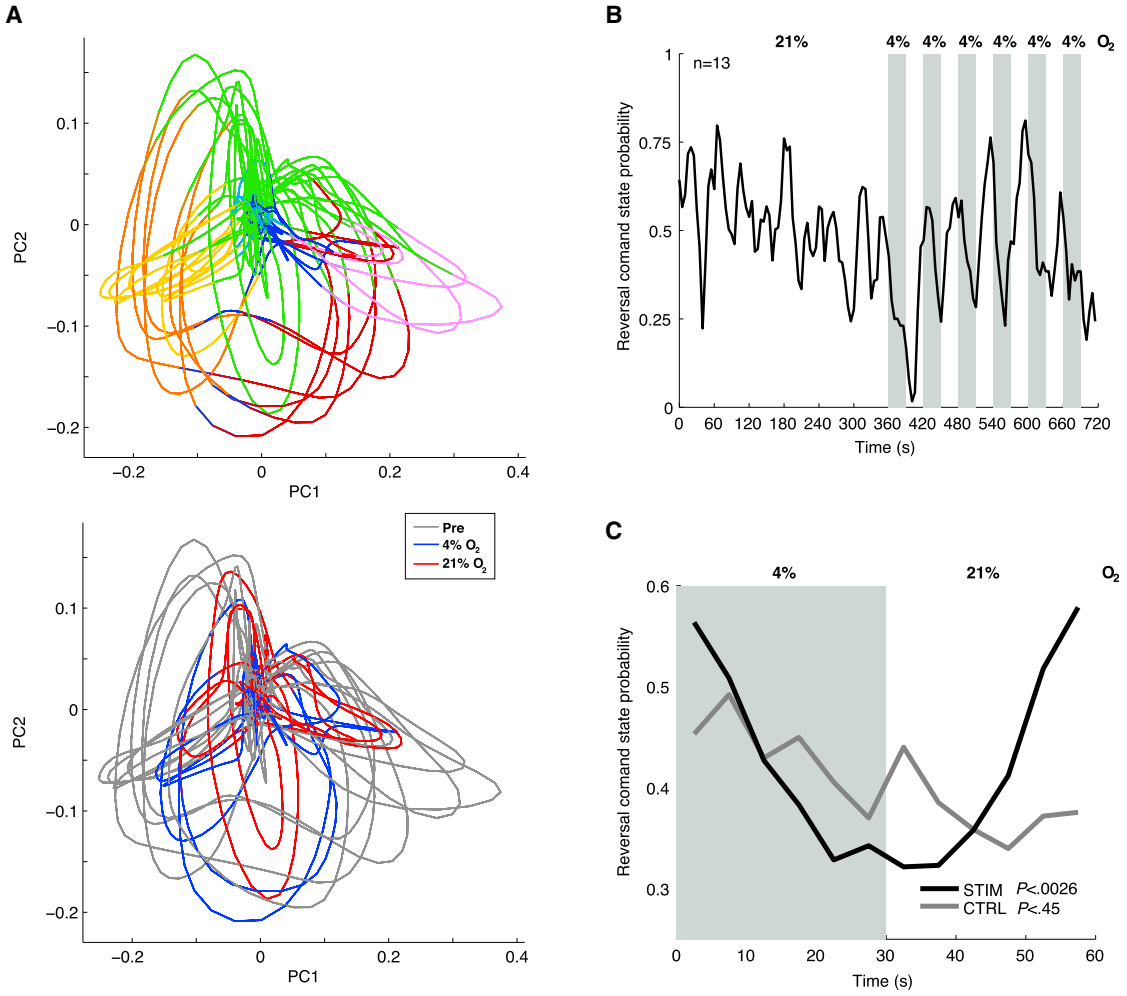

Figure 6. Entrainment of the Global Brain Cycle by Sensory Stimulation

Animals were recorded and stimulated with the oxygen profile indicated in (B).

(A) Phase plots of temporal PCs 1–2 from a representative recording. Top: behavioral command state coloring as in Figure 4B. Bottom: trajectory segments during the pre-stimulus period are labeled gray; segments during the 4% and 21% shift periods are labeled blue and red, respectively.

(B) The trace shows the probability of reversal command state (REVERSAL1 + REVERSAL2 + SUSTAINED REVERSAL) calculated over n = 13 recordings.

(C) Reversal command state probability as in (B) but averaged over the six down- and up-shift periods. p values are calculated by a resampling test and indicate the probability that the stimulus-synced profile shape occurred from a randomly time-shifted stimulus pattern.

See also Figure S7.

cortical areas (Georgopoulos and Carpenter, 2015; Shenoy et al., 2013), and speech in humans (Bouchard et al., 2013) may be sparsely sampled windows onto similarly well-organized, smooth global dynamics.

Our work establishes a framework for future studies aimed at embedding more fine-scaled behaviors beyond the discrete classifications of the state transition diagram, such as gradual steering commands (Iino and Yoshida, 2009) and locomotory gait (Stephens et al., 2008). By exploring more sophisticated sensory input paradigms and studying the animal in different contexts and life stages, we expect that the neural state manifold will be further sub-dividable and support the mapping of other behavioral parameters. Additionally, in-depth analysis of whole-brain activity may uncover previously hidden aspects of behavior; for example, we found two types of reversals (corresponding to RISE1 and RISE2) in whole-brain activity that currently lack known behavioral correlates. Although AVA inhibition had only subtle effects, systematically expanding this approach to other neurons and combinations thereof should reveal whether individual neurons or sub-ensembles are causal to brain dynamics. By probing the system with acute perturbation using optogenetics and imaging at finer timescales and sub-neuronal spatial resolution, it should be possible to uncover the neuronal logic governing trajectory control and branch selection, which underlies decision making in this system. Measuring manifold geometry changes over longer timescales may uncover the characteristics of brain states such as hunger-satiety or sleep-wakefulness.

Our results argue against models of largely feed-forward sensory-to-motor flow where intermediate neuronal layers perform sequential processing and the behavioral state is only ultimately represented within the nervous system at the motor periphery. Instead, our data support a model of an early interface between sensory and motor representations as was suggested by recent single-neuron studies (Hendricks et al., 2012; Luo et al., 2014).

Moreover, motor command representations affect responsiveness of sensory neurons and early interneurons to sensory inputs via feedback mechanisms (Figure S7) that remain to be identified (see also Gordus et al., 2015). Consistent with recent distributed models of sensorimotor action selection in mammals, including primates (Cisek and Kalaska, 2010), our work suggests that the brain's outputs—i.e., its intents and actions—make up a large fraction of its dynamic activity state.

Our findings reveal that a large collection of neuronal classes with distinct morphologies and connectivities (White et al., 1986), distinct molecular compositions and neurotransmitter expression patterns (Hobert, 2013), distinct synaptic transmission properties (Li et al., 2014), and distinct subcellular signal processing capacities (Chalasani et al., 2007; Hendricks et al., 2012; Li et al., 2014) nevertheless collectively share a low-dimensional, pervasive neuronal signal. The class-specific phase relationships with respect to the global brain cycle (Figures S1B and S5) suggest that neurons differentially interact with this shared mode. We therefore propose that the neural state manifold influences and binds local activity to a global reference framework, establishing a consensus that produces stable, coherent behavior.

EXPERIMENTAL PROCEDURES

The Supplemental Experimental Procedures contain more detailed information on each procedure, and in addition, they include descriptions of region of interest detection and neural time series extraction from volumetric Ca^{2+} imaging data, electrophysiology, simulation of nuclear GCaMP signals from voltage traces, population behavior assays, statistics applied in this study, strain genotypes, and molecular biology constructs.

Whole-Brain Ca^{2+} Imaging of *C. elegans* Head Ganglia Neurons

Animals were immobilized with 1 mM tetramisole in microfluidic devices that allow controlled O_2 stimuli as previously described (Schrödel et al., 2013; Zimmer et al., 2009). Recordings were started within 5 min after removal from food. Worms were either imaged for 18 min at constant 21% O_2 or, for the stimulus protocol, imaged for 12 min with the first 6 min at 21% O_2 and the remaining 6 min with 30 s consecutive shifts between 4% and 21% O_2. Data were acquired using an inverted spinning disc microscope (UltraViewVoX, PerkinElmer) equipped with an EMCCD camera (C9100-13, Hamamatsu).

Identification of Head Ganglia Neurons

In each recording, we detected 107–131 neurons, covering 55%–67% of expected neurons in the imaging area. Neurons were identified taking into account their anatomical positions, also in relation to surrounding neurons (http://www.wormatlas.org), and their activity patterns. To confirm ambiguous neuron identities, marker lines expressing red fluorophores in neurons of interest were generated and crossed to the imaging line expressing GCaMP5K pan-neuronally in the nucleus (ZIM504).

Time Series Analysis: PCA, Numerical Differentiation, 4-Phase Segmentation, Phase Timing Analysis, and Clustering

PCA was performed on the time derivatives of $\Delta F/F_0$ neural traces, each normalized by its peak magnitude. To compute de-noised time derivatives without the need of smoothing that can affect precise timing of sharp transitions, the total-variation regularization method (Chartrand, 2011) was applied. To segment individual neuronal activity into 4-phase sequences, first RISE and FALL phases for neurons were identified as periods when the time derivative was greater or lower than a small threshold, respectively. HIGH and LOW phases were then inferred in the remaining gaps. For trajectory segment averaging (Figures 4C, 4D, and S2E) and generation of Movies S2 and S3, neuronal time series were registered to a common phase clock by matching phase segment starts and ends to the reference neuron (AVA or RIM) rise onsets and fall offsets, respectively, followed by linearly interpolating within phase segments. To perform phase timing analysis, first a set of global transitions, either RISE or FALL onsets, were defined by the transitions of a reference neuron (AVA or RIM in this study). Then, relative time delays of the nearest transitions found in other neurons were used to compose a feature vector for each global transition. In the absence of a matching transition within 7 s of the reference neuron transition, a time delay of −10 s was used for the purposes of clustering, since the absence of neurons was also considered an important feature of transitions. *K*-means clustering was applied to transition feature vectors for each full trial using L_1 distance and $k = 2$. Detailed explanations of the above computational analyses may be found in the Supplemental Experimental Procedures.

Behavioral Decoding of Whole-Brain Recordings

Each time point of the phase plot trajectory was first assigned to a global brain cycle HIGH, LOW, RISE1, RISE2, FALL1, or FALL2 segment as described above and in the main text, then mapped to motor command states as follows. RISE1 and RISE 2 segments were mapped to REVERSAL1 and REVERSAL2 command states, respectively. HIGH segments were mapped to the SUSTAINED REVERSAL state. FALL1 and FALL2 segments were mapped to VENTRAL TURN and DORSAL TURN, respectively. LOW segments were mapped to FORWARD except that RIB FALL phases present during global LOW segments were mapped to FORWARD SLOWING command states. A speed drive was assigned to each point on the trajectory as follows, aside from those in SUSTAINED REVERSAL phases for which no speed drive was inferred. During VENTRAL TURN, DORSAL TURN, FORWARD, and FORWARD SLOWING phases, positive speed drive was taken to be the magnitude of RIB activity, normalized to its most negative value during the trial. During REVERSAL1 and 2 phases, negative speed drive was taken to be the derivative of RIM neuron activity, normalized to its highest value during the trial.

Ca^{2+} Imaging in Freely Moving Animals

Ca^{2+} imaging recordings were made using the automatic re-centering system described previously (Faumont et al., 2011) with custom modifications. Young adult worms (0–8 eggs) expressed both mCherry and GCaMP in the neuron of interest. Animals were recorded while freely crawling on agar in a custom built microscope stage containing an airtight chamber with inlet and outlet connectors for gas flow delivery. Images were acquired using two CCD cameras (Evolve 512, Photometrics) connected via a DualCam DC2 beam splitter (Photometrics). A long-distance 63× objective (Zeiss LD Plan-Neofluar 63×, 0.75 NA) was used to obtain unbinned images streamed at 30.3 frames per second (fps) acquisition rate. Simultaneous behavior recordings under infrared illumination (780 nm) were made using a CCD camera (Manta Prosilica GigE, Applied Vision Technologies) at 4× magnification and 10 fps acquisition rate.

SUPPLEMENTAL INFORMATION

Supplemental Information includes Supplemental Experimental Procedures, seven figures, one table, and three movies and can be found with this article online at http://dx.doi.org/10.1016/j.cell.2015.09.034.

AUTHOR CONTRIBUTIONS

S.K. designed experiments, developed analytical methods for whole-brain imaging datasets, and analyzed data. H.S.K. designed experiments, generated transgenic strains, performed Ca^{2+}-imaging experiments in freely moving animals, developed analytical methods, and analyzed data. T.S. designed

experiments, generated transgenic strains, performed whole-brain imaging experiments, and analyzed data. S.S. performed population behavioral recordings and analyzed data. T.H.L. and S.L. performed electrical recordings; E.Y. wrote code for behavioral analysis; and M.Z. designed experiments, developed analytical methods, and led the project. S.K., H.S.K., T.S., and M.Z. wrote the manuscript.

ACKNOWLEDGMENTS

We thank Cori Bargmann, Larry Abbott, Alipasha Vaziri, Andrew Straw, Hagai Lalazar, Omri Barak, and Sean Escola for critically reading the manuscript, Richard Latham for technical support, and Martin Colombini for manufacturing of mechanical components. The research leading to these results has received funding from the European Community's Seventh Framework Programme (FP7/2007-2013)/ERC grant agreement number 281869 (acronym: *elegans Neurocircuits*) to M.Z., the Simons Foundation (grant number 324958 to M.Z.), an EMBO Long Term Fellowship to S.K. (number ALTF 345-2014), an NIH training grant to T.H.L. (number F31 NS061697), an NIH T32 training grant to E.Y. (number T32 MH015174-38), and the Research Institute of Molecular Pathology (IMP). The IMP is funded by Boehringer Ingelheim.

Received: July 2, 2015
Revised: August 14, 2015
Accepted: September 2, 2015
Published: October 15, 2015

REFERENCES

Ahrens, M.B., Li, J.M., Orger, M.B., Robson, D.N., Schier, A.F., Engert, F., and Portugues, R. (2012). Brain-wide neuronal dynamics during motor adaptation in zebrafish. Nature *485*, 471–477.

Ahrens, M.B., Orger, M.B., Robson, D.N., Li, J.M., and Keller, P.J. (2013). Whole-brain functional imaging at cellular resolution using light-sheet microscopy. Nat. Methods *10*, 413–420.

Anderson, D.J., and Perona, P. (2014). Toward a science of computational ethology. Neuron *84*, 18–31.

Bouchard, K.E., Mesgarani, N., Johnson, K., and Chang, E.F. (2013). Functional organization of human sensorimotor cortex for speech articulation. Nature *495*, 327–332.

Briggman, K.L., Abarbanel, H.D., and Kristan, W.B., Jr. (2005). Optical imaging of neuronal populations during decision-making. Science *307*, 896–901.

Bruno, A.M., Frost, W.N., and Humphries, M.D. (2015). Modular deconstruction reveals the dynamical and physical building blocks of a locomotion motor program. Neuron *86*, 304–318.

Busch, K.E., Laurent, P., Soltesz, Z., Murphy, R.J., Faivre, O., Hedwig, B., Thomas, M., Smith, H.L., and de Bono, M. (2012). Tonic signaling from O_2 sensors sets neural circuit activity and behavioral state. Nat. Neurosci. *15*, 581–591.

Chalasani, S.H., Chronis, N., Tsunozaki, M., Gray, J.M., Ramot, D., Goodman, M.B., and Bargmann, C.I. (2007). Dissecting a circuit for olfactory behaviour in Caenorhabditis elegans. Nature *450*, 63–70.

Chalfie, M., Sulston, J.E., White, J.G., Southgate, E., Thomson, J.N., and Brenner, S. (1985). The neural circuit for touch sensitivity in Caenorhabditis elegans. J. Neurosci. *5*, 956–964.

Chartrand, R. (2011). Numerical differentiation of noisy, nonsmooth data. ISRN Applied Mathematics *2011*, 1–11.

Churchland, M.M., Cunningham, J.P., Kaufman, M.T., Foster, J.D., Nuyujukian, P., Ryu, S.I., and Shenoy, K.V. (2012). Neural population dynamics during reaching. Nature *487*, 51–56.

Cisek, P., and Kalaska, J.F. (2010). Neural mechanisms for interacting with a world full of action choices. Annu. Rev. Neurosci. *33*, 269–298.

Cunningham, J.P., and Yu, B.M. (2014). Dimensionality reduction for large-scale neural recordings. Nat. Neurosci. *17*, 1500–1509.

Dankert, H., Wang, L., Hoopfer, E.D., Anderson, D.J., and Perona, P. (2009). Automated monitoring and analysis of social behavior in Drosophila. Nat. Methods *6*, 297–303.

Donnelly, J.L., Clark, C.M., Leifer, A.M., Pirri, J.K., Haburcak, M., Francis, M.M., Samuel, A.D.T., and Alkema, M.J. (2013). Monoaminergic orchestration of motor programs in a complex C. elegans behavior. PLoS Biol. *11*, e1001529.

Faumont, S., Rondeau, G., Thiele, T.R., Lawton, K.J., McCormick, K.E., Sottile, M., Griesbeck, O., Heckscher, E.S., Roberts, W.M., Doe, C.Q., and Lockery, S.R. (2011). An image-free opto-mechanical system for creating virtual environments and imaging neuronal activity in freely moving Caenorhabditis elegans. PLoS ONE *6*, e24666.

Georgopoulos, A.P., and Carpenter, A.F. (2015). Coding of movements in the motor cortex. Curr. Opin. Neurobiol. *33*, 34–39.

Gordus, A., Pokala, N., Levy, S., Flavell, S.W., and Bargmann, C.I. (2015). Feedback from network states generates variability in a probabilistic olfactory circuit. Cell *161*, 215–227.

Gray, J.M., Hill, J.J., and Bargmann, C.I. (2005). A circuit for navigation in Caenorhabditis elegans. Proc. Natl. Acad. Sci. USA *102*, 3184–3191.

Grillner, S. (2006). Biological pattern generation: the cellular and computational logic of networks in motion. Neuron *52*, 751–766.

Ha, H.I., Hendricks, M., Shen, Y., Gabel, C.V., Fang-Yen, C., Qin, Y., Colón-Ramos, D., Shen, K., Samuel, A.D.T., and Zhang, Y. (2010). Functional organization of a neural network for aversive olfactory learning in Caenorhabditis elegans. Neuron *68*, 1173–1186.

Harvey, C.D., Coen, P., and Tank, D.W. (2012). Choice-specific sequences in parietal cortex during a virtual-navigation decision task. Nature *484*, 62–68.

Hendricks, M., Ha, H., Maffey, N., and Zhang, Y. (2012). Compartmentalized calcium dynamics in a C. elegans interneuron encode head movement. Nature *487*, 99–103.

Hobert, O. (2013). The neuronal genome of Caenorhabditis elegans (WormBook), pp. 1–106.

Iino, Y., and Yoshida, K. (2009). Parallel use of two behavioral mechanisms for chemotaxis in Caenorhabditis elegans. J. Neurosci. *29*, 5370–5380.

Jin, X., Tecuapetla, F., and Costa, R.M. (2014). Basal ganglia subcircuits distinctively encode the parsing and concatenation of action sequences. Nat. Neurosci. *17*, 423–430.

Jolliffe, I.T. (2002). Principal Component Analysis, Second Edition (Springer).

Kawano, T., Po, M.D., Gao, S., Leung, G., Ryu, W.S., and Zhen, M. (2011). An imbalancing act: gap junctions reduce the backward motor circuit activity to bias C. elegans for forward locomotion. Neuron *72*, 572–586.

Kimata, T., Sasakura, H., Ohnishi, N., Nishio, N., and Mori, I. (2012). Thermotaxis of C. elegans as a model for temperature perception, neural information processing and neural plasticity. Worm *1*, 31–41.

Laurent, P., Soltesz, Z., Nelson, G.M., Chen, C., Arellano-Carbajal, F., Levy, E., and de Bono, M. (2015). Decoding a neural circuit controlling global animal state in C. elegans. eLife *4*, 4.

Lemon, W.C., Pulver, S.R., Höckendorf, B., McDole, K., Branson, K., Freeman, J., and Keller, P.J. (2015). Whole-central nervous system functional imaging in larval Drosophila. Nat. Commun. *6*, 7924.

Li, Z., Liu, J., Zheng, M., and Xu, X.Z.S. (2014). Encoding of both analog- and digital-like behavioral outputs by one C. elegans interneuron. Cell *159*, 751–765.

Luo, L., Wen, Q., Ren, J., Hendricks, M., Gershow, M., Qin, Y., Greenwood, J., Soucy, E.R., Klein, M., Smith-Parker, H.K., et al. (2014). Dynamic encoding of perception, memory, and movement in a C. elegans chemotaxis circuit. Neuron *82*, 1115–1128.

Mante, V., Sussillo, D., Shenoy, K.V., and Newsome, W.T. (2013). Context-dependent computation by recurrent dynamics in prefrontal cortex. Nature *503*, 1–19.

Marder, E., and Bucher, D. (2007). Understanding circuit dynamics using the stomatogastric nervous system of lobsters and crabs. Annu. Rev. Physiol. *69*, 291–316.

Panier, T., Romano, S.A., Olive, R., Pietri, T., Sumbre, G., Candelier, R., and Debrégeas, G. (2013). Fast functional imaging of multiple brain regions in intact zebrafish larvae using selective plane illumination microscopy. Front. Neural Circuits *7*, 65.

Pierce-Shimomura, J.T., Morse, T.M., and Lockery, S.R. (1999). The fundamental role of pirouettes in Caenorhabditis elegans chemotaxis. J. Neurosci. *19*, 9557–9569.

Pokala, N., Liu, Q., Gordus, A., and Bargmann, C.I. (2014). Inducible and titratable silencing of Caenorhabditis elegans neurons in vivo with histamine-gated chloride channels. Proc. Natl. Acad. Sci. USA *111*, 2770–2775.

Prevedel, R., Yoon, Y.-G., Hoffmann, M., Pak, N., Wetzstein, G., Kato, S., Schrödel, T., Raskar, R., Zimmer, M., Boyden, E.S., and Vaziri, A. (2014). Simultaneous whole-animal 3D imaging of neuronal activity using light-field microscopy. Nat. Methods *11*, 727–730.

Schrödel, T., Prevedel, R., Aumayr, K., Zimmer, M., and Vaziri, A. (2013). Brain-wide 3D imaging of neuronal activity in Caenorhabditis elegans with sculpted light. Nat. Methods *10*, 1013–1020.

Seeds, A.M., Ravbar, P., Chung, P., Hampel, S., Midgley, F.M., Jr., Mensh, B.D., and Simpson, J.H. (2014). A suppression hierarchy among competing motor programs drives sequential grooming in Drosophila. eLife *3*, e02951.

Shenoy, K.V., Sahani, M., and Churchland, M.M. (2013). Cortical control of arm movements: a dynamical systems perspective. Annu. Rev. Neurosci. *36*, 337–359.

Stephens, G.J., Johnson-Kerner, B., Bialek, W., and Ryu, W.S. (2008). Dimensionality and dynamics in the behavior of C. elegans. PLoS Comput. Biol. *4*, e1000028.

Varshney, L.R., Chen, B.L., Paniagua, E., Hall, D.H., and Chklovskii, D.B. (2011). Structural properties of the Caenorhabditis elegans neuronal network. PLoS Comput. Biol. *7*, e1001066.

Wen, Q., Po, M.D., Hulme, E., Chen, S., Liu, X., Kwok, S.W., Gershow, M., Leifer, A.M., Butler, V., Fang-Yen, C., et al. (2012). Proprioceptive coupling within motor neurons drives C. elegans forward locomotion. Neuron *76*, 750–761.

White, J.G., Southgate, E., Thomson, J.N., and Brenner, S. (1986). The structure of the nervous system of the nematode Caenorhabditis elegans. Philos. Trans. R. Soc. Lond. B Biol. Sci. *314*, 1–340.

Zimmer, M., Gray, J.M., Pokala, N., Chang, A.J., Karow, D.S., Marletta, M.A., Hudson, M.L., Morton, D.B., Chronis, N., and Bargmann, C.I. (2009). Neurons detect increases and decreases in oxygen levels using distinct guanylate cyclases. Neuron *61*, 865–879.